Proceedings of the ASME 2022 International Design Engineering Technical Conferences & Computers and Information in Engineering Conference
IDETC/CIE 2022
August 14-August 17, 2022, St. Louis Missouri, USA

DETC2022-89030

STRESS TRAJECTORY GUIDED STRUCTURAL DESIGN AND TOPOLOGY OPTIMIZATION

Junpeng Wang*
Computer Graphics and Visualization
Department of Informatics
Technical University of Munich
Garching 85748, Germany
Email: junpeng.wang@tum.de

Jun Wu
Department of Sustainable
Design Engineering
Delft University of Technology
Delft 2628 CE, The Netherlands
Email: j.wu-1@tudelft.nl

Rüdiger Westermann
Computer Graphics and Visualization
Department of Informatics
Technical University of Munich
Garching 85748, Germany
Email: westermann@tum.de

ABSTRACT

Density-based topology optimization using global and local volume constraints is a key technique to automatically design lightweight structures. It is known that stiffness optimal structures comprise spatially varying geometric patterns that span multiple length scales. However, both variants of topology optimization have challenges to efficiently converge to such a structural layout. In this paper, we investigate material layouts that are generated from stress trajectories, i.e., to compile a globally consistent structure by tracing the stress trajectories from finite element simulation of the solid design domain under external loads. This is particularly appealing from a computational perspective, since it avoids iterative optimization that involves finite element analysis on fine meshes. By regularizing the thickness of each trajectory using derived strain energy measures along them, stiff structural layouts can be generated in a highly efficient way. We then shed light on the use of the resulting structures as initial density fields in density-based topology optimization, i.e., to generate an initial density field that is then further optimized via topology optimization. We demonstrate that by using a stress trajectory guided density initialization in lieu of a uniform density field, convergence issues in density-based topology optimization can be significantly relaxed at comparable stiffness of the resulting structural layouts.

*Address all correspondence to this author.

1 Introduction

The design of optimal lightweight structures is a fundamental research topic in design engineering. It is known that stiffness optimal structures, i.e., with minimum compliance measured by strain energy, comprise spatially varying geometric patterns that span multiple length scales [1]. To approach theoretically optimal structures, early works in topology optimization (e.g. [2]) explored a material model corresponding to infinitely small square cells with rectangular holes. The resulting multi-scale structures were deemed challenging for manufacturing. This had promoted the field of topology optimization to shift its focus from homogenization-based approaches to "mono-scale" approaches that optimize the distribution of a homogeneous isotropic material [3,4,5], e.g., using a material model known as Solid Isotropic Material with Penalization.

Due to the increasing flexibility of additive manufacturing (AM), recent years saw a resurgent interest in optimal design of multi-scale structures. AM is effective for fabricating complex mono-scale structures as well as delicate multi-scale structures such as infill lattices. We refer to a recent review article for the history and latest developments in topology optimization of multi-scale structures [1]. Among these approaches, it is of particular interest to adapt the lattice orientation according to stress directions. Topology optimization approaches for designing conforming lattice structures can be categorised into two groups: full-scale density-based topology optimization using local volume constraints [6], and de-homogenization of optimized,

locally defined orientations [7, 8].

Density-based approaches. Density-based topology optimization commonly starts from a homogeneous initial density field and then iteratively performs finite element simulation of the current material distribution to optimize for structural performance, under a constraint on the total material volume. Since the theoretically optimal structures are multi-scale, the density-based approach in principle shall be able to achieve these multi-scale structures. This, however, is only possible by using sufficiently fine meshes for discretizing the material distribution, and requires careful continuation techniques. Therefore, commonly seen topology optimization results are predominantly mono-scale.

To promote the appearance of fine scale substructures, local volume constraints have been proposed to replace the total volume constraint [6]. This results in distributed substructures spreading across the design domain, which largely follow the principal stress directions. This approach has been extended in various directions, for instance, to design concurrently structures and porous substructures therein [9], porous structures with gradation in the porosity and pore size [10, 11], fiber-reinforced structures [12], and to incorporate multiple materials [13] and self-supporting constraints [14]. Lately, as demonstrated by Wang et al. [15], convergence issues may arise in the regions enclosing degenerate points in the stress field, i.e., points where the eigenvalues indicating major and minor stress direction become indistinguishable. To reduce the number of optimization iterations in these cases, Wang et al. proposed using the topological skeleton, i.e., principal stress trajectories connecting pairs of degenerate points, of the stress field in the solid object under load to initialize the density field.

De-homogenization. In the seminal work of Bendsøe and Kikuchi, they proposed a material model for infinitely small square cells with rectangular hole [2]. Using numerical homogenization to evaluate equivalent mechanical properties of these cells, one can optimize the spatially varying size as well as orientation of such cells. The challenge that is addressed by de-homogenization is to compile a globally consistent structure from these locally defined unit cell configurations. Pantz et al proposed one of the first solutions towards this end [7], which has been further developed [8, 16, 17]. A key component in these approaches is to seek a scalar field, whose gradient is aligned with the optimized orientation. An effective alternative is to use hexahedral meshing to create meshes with edges aligned to the optimized orientation [18].

In this work, we investigate material layouts that are generated from stress trajectories, i.e., to compile a globally consistent structure by tracing the stress trajectories from finite element simulation of the solid design domain under external loads. This is particularly appealing from a computational perspective, since it avoids iterative optimization involving finite element analysis on fine meshes. On this aspect, it is in line with the de-homogenization approaches. Similar ideas to tracing stress lines have been explored in [19, 20, 21, 22], yet a challenge is to get a (quasi-)uniform distribution of the stress lines. To generate such layouts, we exploit recent results in trajectory-based stress visualization [23], which automatically generate a regular, smoothly varying, and space-filling structure consisting of trajectories along the major and minor principal stress directions. The thickness of each trajectory can be further regularized by using derived strain energy measures along them. By converting the resulting trajectory ensemble to a corresponding density field, stiff structural layouts can be generated in a highly efficient way.

We then shed light on the use of the resulting structures as initial density fields in density-based topology optimization, i.e., to generate an initial density field that is then optimized via topology optimization. In density-based approaches, as with other topology optimization approaches, the results are heavily influenced by the initialization, both in terms of convergence and optimality of the optimized structural layout. This is because topology optimization is a non-convex problem, and depending on the initialization a different local optimum is reached. We demonstrate that by using a material initialization guided by stress trajectories instead of a uniform density field, convergence issues in density-based topology optimization can be significantly relaxed at comparable stiffness of the resulting layouts. In an exhaustive study we compare the layouts generated by all variants regarding their mechanical properties and computational cost.

The rest of our paper is organized as follows. In Section 2 we present the method to generate space-filling stress trajectories. The use of these stress trajectories for structural design and for topology optimization is presented in Sections 3 and 4, respectively. We then discuss the computational and structural performance of different variants in Section 5, before concluding the paper in Section 6.

2 Principal stress trajectories

A consistent visual representation of a 2D stress tensor field can be obtained via principal stress trajectories, which convey the directions of the principal stresses and are used in particular to show where and how loads are internally redirected and deflected. We will subsequently call such trajectories Principal Stress Lines (PSLs).

At each point in a 2D solid under load, the stress state is fully described by the stress vectors for two mutually orthogonal orientations. The second-order stress tensor

$$S(x,y) = \begin{bmatrix} \sigma_{xx} & \tau_{xy} \\ \tau_{xy} & \sigma_{yy} \end{bmatrix}_{(x,y)} \tag{1}$$

contains these vectors for the axes of a Cartesian coordinate system. σ_{xx} and σ_{yy} are the normal stress components along the x and y direction, respectively, τ_{xy} is the shear stress component.

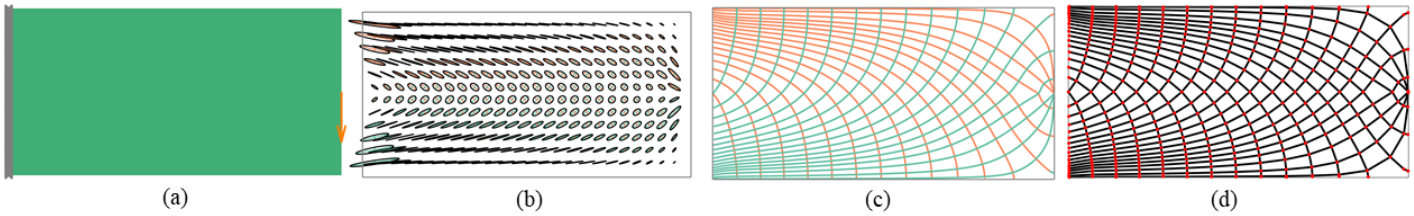

FIGURE 1. (a) Solid model discretized by 500×250 simulation elements. Gray and orange arrowheads, respectively, indicate fixation and loading conditions. (b) Tensor glyphs show the principal stress directions. Red and green, respectively, indicate positive and negative principal stresses. (c) Uniformly distributed PSLs. Orange and turquoise trajectories represent the major and minor principal stress directions, respectively. (d) Red dots indicate PSL intersections, and curved PSLs are converted into piecewise linear segments.

S is symmetric since the shear stresses are equal on mutually orthogonal lines. The principal stress directions of the stress tensor are given by the eigenvectors of S, indicating the two mutually orthogonal directions along which the shear stresses vanish. The corresponding eigenvalues σ_1 and σ_2 of S represent the magnitudes of the principal stresses. For $\sigma_1 \geq \sigma_2$, σ_1 is called the major principal stress, and σ_2 the minor principal stress, and the corresponding eigenvectors v_1 and v_2 are called major and minor principal stress directions. The signs of the principal stress magnitudes classify the stresses into tension (positive sign) or compression (negative sign). Since there are two principal stresses acting at each point, the classification is with respect to a specific direction. Figs. 1a,b, respectively, show a 2D solid under external loads and the principal stresses via elliptical tensor glyphs. The semi-major and -minor axes of the ellipses correspond to the major and minor principal stress directions.

PSLs are the trajectories that are everywhere tangent to either the major or the minor principal stress direction. They are computed by numerically integrating massless particles in each single (normalized) eigenvector field (see Fig. 1c). PSLs are started from an arbitrary seed points, and integrated until the domain boundary is reached, the PSL performs a loop, i.e. comes closer to a previous point than a predefined distance threshold, or the number of integration steps exceeds a user-defined bound. A Runge-Kutta (RK2) scheme with fixed integration step size δ is used for numerical integration. In each integration step, the stress tensor T is interpolated and the eigenvalues and eigenvectors are computed from the interpolated tensor. The next integration step is performed in the direction with the least deviation from the previous direction.

In addition to the regular PSLs, there are special PSLs comprising the so-called topological skeleton. These PSLs start from a degenerate point of the stress tensor field and separate areas of different stress behavior. Degenerate points are characterized by two equal eigenvalues, so that the principal directions cannot be decided. In the vicinity of such points a set of hyperbolic and parabolic sectors exist, in which similar patterns of neighboring trajectories are observed [24]. The topological skeleton consists of the boundaries between adjacent sectors—so-called separatrices—and indicate pathways along which the forces are steered towards the degenerate points. To extract the topological skeleton, first the locations of degenerate points are computed by using the invariant formulation by Delmarcelle and Hesselink [24], and then PSLs are started from these points (see Figs. 5h,i for an example including the topological skeleton).

2.1 Uniformly distributed stress trajectories

To generate a uniformly distributed set of PSLs, we use the publicly available visualization tool for 3D stress fields provided by Wang et al. [23] [1]. Designed for extracting and visualizing the PSLs along the three mutually orthogonal principal stress directions in 3D solids under load, with only minor modifications the tool can be adapted to work with 2D objects.

Starting with a set of seed points that are uniformly distributed across the domain, PSL extraction starts by selecting one of the candidate seed points and tracing the major and minor PSLs (the seed PSLs) passing through it. The point is then classified as visited by major and minor PSLs. All remaining seed points that have not yet been classified as major and minor, and are closer to a new PSL than a threshold ϑ, are processed in the following way: Firstly, the coordinate of such a point is set (i.e., snapped) to the coordinate of the closest integration point on the PSL (in the first step, the closest PSL of the seed PSLs). Secondly, if the new PSL is a major PSL, the classification major is added to the point, and minor if the new PSL is a minor PSL. Then, the seed point that is closest to the initial seed point and not yet classified as major and minor is selected, and a major (minor) PSL is traced if the point is classified as minor (major). *Snapping*, *classification*, and *selection* are then repeated until all points are classified as major and minor. By this procedure it is ensured that around each PSL a band is generated from which no more PSL is seeded, and new PSLs are always seeded from points on existing PSLs. This generates a fairly uniform and space-filling distribution of PSLs (see Fig. 1c and Fig. 5).

[1] https://github.com/Junpeng-Wang-TUM/3D-TSV

To include the topological skeleton, it is first extracted and all separatrices are considered as seed PSLs as described before.

2.2 Piecewise linear PSLs

Each PSL is a curved trajectory in the 2D domain, composed of a set of integration points that are connected via line segments. Especially if the density of PSLs is low, PSLs tend to curve strongly between two intersection points with other PSLs. When using PSLs to generate an initial density field in which the material is smeared out along them, curved segments require more material than straight lines and are less stable than lines. Therefore, after all PSLs are computed, we compute all intersection points between PSLs and convert each PSL into a polyline comprised of intersection points and linear connections between them. The result of this process is shown in Fig. 1d.

To efficiently compute piecewise linear PSLs, the following extensions are introduced: Firstly, once a PSL is computed, the integration points along this PSL are assigned an index relative to one of the end points of that PSL, i.e., an index I_i^{id} says that the point is the i-th point when counting from the selected end point of the PSL with unique identifier id. Secondly, additional information is stored at the cells of the simulation grid on which stresses are simulated. At every cell a PSL is passing through, the identifier of the PSL is stored. Thus, eventually each cell contains the identifiers of all PSLs that might intersect in this cell. Since only intersections between major and a minor PSLs can occur, all cells with at least one identifier of a major PSL and a minor PSL are considered, and the intersection points between the major and minor PSLs are computed. This results in line-line intersection test to obtain the locations of intersection points. In addition, for each intersection point the indices of that point along the PSLs it resides on are computed by linear interpolation of the indices at the line end points. Each PSL stores a separate list containing all intersection points that are found along it, so that by sorting these lists with respect to increasing index a sorted sequence of intersection points is obtained.

3 PSL-guided structural design

In the following, we describe how a density field is obtained from the set of piecewise linear PSLs. This density field is then used in a finite element stress simulation to compute the compliance of the layout. In the following chapters, this layout is then used as initial density field in topology optimization, and the results are compared regarding their mechanical properties.

Given the current and next point along a piecewise linear PSL, we use Bresenham line rasterization to compute all simulation cells that are hit by the line connecting both points. These cells are then set to solid, and the process moves on to the next pair of points along the PSL. The result of the rasterization is shown in Fig. 2a.

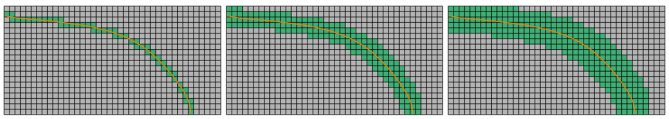

(a) $t = 1$. (b) $t = 2$. (c) $t = 3$.

FIGURE 2. Material layout via PSL rasterization. From (b) to (c), the thickness of the initial material structure in (a) is increased by morphological dilation.

The material layout can be flexibly and efficiently adjusted by using a lower or higher density of the computed PSLs. Concrete timings for PSL extraction depending on the resolution of the simulation grid and the PSL density are given in Sec. 5. When smearing out the material along the PSLs as described, rather thin structures are generated and the overall compliance of the layout is only acceptable if many PSLs are used. To address this limitation, the material structures can be thickened via a morphological dilation using a 3×3 structuring element, i.e., around each solid cell also the 8 adjacent cells are made solid. This process can be applied iteratively to increase the PSL thickness further (see Figs. 2b,c). Next, we describe an approach to automatically adapt the thickness of each PSL by considering a PSL's importance regarding the overall compliance.

3.1 Strain energy guided thickness control

Automatic thickness control aims at using the prescribed material budget in the most effective way so that a low compliance is achieved. Therefore, the importance of each PSL for reducing the compliance is used as an indicator of the PSL's thickness. The overall compliance of a material layout is computed via the strain energies of the elements in the simulation grid, i.e., by adding the strain energies of all solid elements in the domain. The overall compliance per PSL can be computed by adding the strain energies of all elements covered by a PSL. In this way, the contribution of each PSL to the overall compliance, i.e. to resist the external loads, can be quantified. Specifically, the stored strain energy of the i-th PSL is computed as

$$c_{T_i} = \sum_{k=1}^{M_k} c_e. \tag{2}$$

Where M_k is the number of elements covered by the PSL. To avoid that the importance of a PSL is dominated by its length, c_{T_i} is finally divided by the number of elements directly intersected by the PSL. The resulting values are then used to guide the adjustment of each PSL's thickness.

Material initialization starts by setting the initial PSL thickness (t_0) either to 2, i.e., at least there are three layers of cells surrounding the PSL (see Fig. 2b), or to a larger value specified

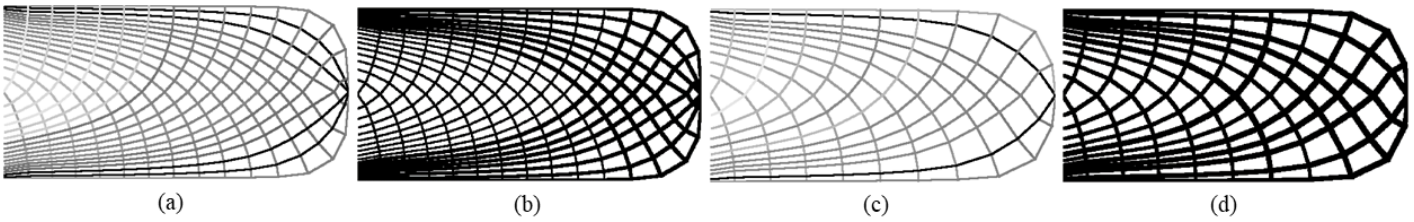

FIGURE 3. PSL-guided material layouts for two different PSL densities, with the used volume fractions (v) and resulting compliances (c). (a) ($v = 0.370$, $c = 2.657c_0$) and (c) ($v = 0.250$, $c = 4.436c_0$): Layouts using PSLs with $t_0 = 2$, decreasing brightness indicates increasing PSL strain energy. (b) ($v = 0.493$, $c = 1.839c_0$) and (d) ($v = 0.499$, $c = 1.780c_0$): layouts corresponding to (a) and (c) where thickness is adapted according to strain energy. $c_0 = 40.93$ is the compliance of the fully solid domain.

by the user. This enables to consider manufacturing constraints, for instance, to enforce a certain minimum thickness that is required by the printing process. Furthermore, a maximum thickness t_{max} is set to reduce the chance that adjacent PSLs merge and form thick strands. Now, in the case that the usable material budget α_{global} has not been reached by the initial material layout, in descending order with respect to c_{T_i} the PSL's thickness is set to t_{max} until all material has been deposited. Thus, a final layout comprising PSL-guided material structures with either the minimum or maximum allowed thickness are generated. We also performed tests using an assignment strategy that generates structures with thickness values within the whole range from t_0 to t_{max}, yet while this improved the overall compliance only marginally it increased the computational overhead considerably.

For two initial material layouts using different PSL densities, Figs. 3a,c show the importance values that are computed per PSL by greyscales ranging from bright (low importance) to dark (high importance). Figures 3b,d show the corresponding final layouts after automatic thickness control. The finite element simulation is then re-performed using the empty-solid material design to evaluate the mechanical performance of the layout. It can be seen that adaptive thickness control distributes the material along regions that are important for achieving mechanically sound layouts and improves the overall compliance.

4 PSL-guided structural topology optimization

In density-based topology optimization, the design variable is the pseudo density of each element in the discretized design space. A structural layout can be represented by a binary field, i.e., density ρ_e equals 0 or 1, indicating an empty or solid element. The objective is to find the stiffest structure, i.e., minimum compliance, for a prescribed set of boundary conditions, and under an upper bound on the global material fraction,

$$\frac{1}{n}\sum_e \rho_e \leq \alpha_{\text{global}}. \tag{3}$$

Here n is the number of elements, and α_{global} is the global material fraction.

To solve the optimization problem by mathematical programming, the binary variables are relaxed to take intermediate values between 0 and 1. The Young's modulus associated with intermediate density values ($E_e(\rho_e)$) is interpolated from that of a solid basis element E_0 (i.e., $\rho_0 = 1$).

$$E_e(\rho_e) = \rho_{\min} + \rho_e^p E_0. \tag{4}$$

$\rho_{\min}$ is a non-zero small value, to avoid the stiffness matrix becoming singular, typically $\rho_{\min} = 10^{-6}$. The power p is a key parameter for the validity of the optimized layout. $p = 1$ results in a convex optimization problem, but it overestimates the attainable Young's modulus for intermediate densities (cf. Hashin–Shtrikman bounds [25]). The resulting optimized layout consists of many intermediate density values, i.e. large grey regions when visualizing the layout as an image. $p = 3$ is a reasonable approximation of the Hashin–Shtrikman bounds [26], according to which, for instance, half density ($\rho_e = 0.5$) gets much less than half Young's modulus. This physically valid interpolation thus promotes the optimization to converge to a physically valid structural layout (i.e., a binary density field). $p > 1$, however, raises a challenge for mathematical programming as the optimization problem becomes non-convex. Given the fact that the number of design variables in topology optimization is large, there exist an extremely large number of local minima.

Strictly speaking, to approach theoretically optimal structures, one shall start with $p = 1$, and gradually increase its value after some iterations, until p eventually reaches 3. Practically, to cut down the number of iterations, one commonly starts directly with $p = 3$ (e.g., in the 99-line or 88-line Matlab versions [27, 28]). Meanwhile since the discretization resolution of the design space is limited, the optimized structural layout, under a global material volume constraint, often consists of distinctively bulk substructures (cf Fig. 4a) rather than a multi-scale structure.

To design bone-inspired porous structures, Wu et al. pro-

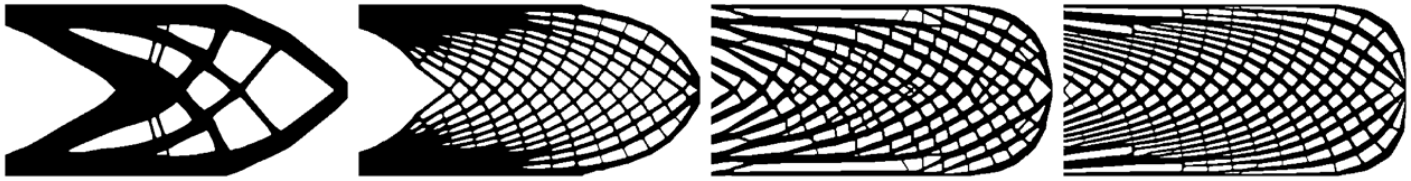

(a) $c = 1.541c_0, v = 0.500$, $s = 6.0 \times 10^{-3}, N = 281$. (b) $c = 1.543c_0, v = 0.500$, $s = 3.1 \times 10^{-3}, N = 281$. (c) $c = 1.901c_0, v = 0.530$, $s = 9.9 \times 10^{-3}, N = 433$. (d) $c = 1.801c_0, v = 0.549$, $s = 7.3 \times 10^{-3}, N = 281$.

FIGURE 4. (a), (c): Structural layouts generated via topology optimization with global and local volume constraint, respectively, starting with a homogeneous density field. (b), (d): Corresponding results when the initial density field is guided by PSLs, i.e., higher initial density is distributed along the PSLs in Fig. 3a, and lower initial density is prescribed in all other regions. c is the compliance and c_0 is the compliance of a fully solid domain, v is the deposition ratio. s is the sharpness value introduced in Sec. 5, where a smaller value indicates a sharper binary layout. N represents the number of iterations until s is reached.

posed to replace the global volume constraint with local volume constraints [6]. A local volume constraint is applied to each element, i.e.,

$$\bar{\rho}_e \leq \alpha_e, \ \forall e \tag{5}$$

where α_e is a prescribed upper bound on the local volume. $\bar{\rho}_e$ is the average of densities in a small region centered at the centroid of element e, computed by

$$\bar{\rho}_e = \frac{\sum_{i \in N_e} \rho_i}{\sum_{i \in N_e} 1}, \quad N_e = \{i | \parallel x_i - x_e \parallel_2 \leq R_e\}, \ \forall e, \tag{6}$$

where R_e denotes the radius of a circular region. x_i and x_e represent the centroid of elements, N_e represents the number of elements within this circular region.

Figure 4c shows an example of using the local volume constraint. The optimization problem is solved using the method of moving asymptotes (MMA) [29]. We refer to Wu et al. [6] for a detailed discussion of the computational steps for avoiding checkerboard patterns and stimulating a 0-1 design. The local volume constraints are more restrictive than the global volume constraint. Consequently, the optimized structure with the same amount of total material is somewhat less stiff than obtained with the global constraint. The benefits of the porous structures include robustness regarding material damage, unmodelled variation in boundary conditions, and buckling.

Density-based topology optimization under either global or local volume constraints is dependent on the initialization of the density field. Commonly in density-based topology optimization, one prescribes $\rho_e = \alpha_{\text{global}}$ or $\alpha_e, \forall e$, for global or local volume constraints, respectively.

We propose to use a PSL-guided density field to initialize $\boldsymbol{\rho}^{[0]}$. In particular, we use the PSL-guided layouts as shown in Figs. 3a,c for initialization. Here the elements corresponding to the thickened PSLs ($\mathscr{P}$) are prescribed a higher initial value ($\rho^{[0]}_{e \in \mathscr{P}} = 1$ in this paper). The rest elements have a lower value, $\rho^{[0]}_{e \notin \mathscr{P}} = \alpha_{\text{global}}$ or α_e. Thus, the PSL trajectories are pre-embedded into the $\boldsymbol{\rho}^{[0]}$. Figures 4a,b compare optimized layouts using a homogeneous initialization and the proposed initialization, under the global volume constraint. Figures 4c,d compare the effects of initialization for local volume constraints.

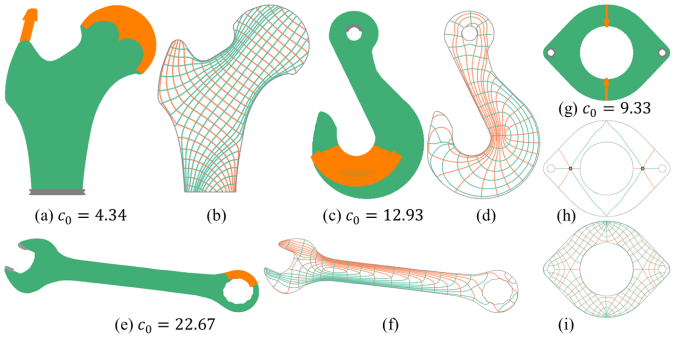

FIGURE 5. Models used in our experiments. Grey regions and orange arrowheads indicate fixations and loads, respectively. c_0 is the compliance of the fully solid layout under the boundary conditions. Orange and turquoise trajectories represent the major and minor PSLs, respectively. In (h), the topological skeleton that is traced from the two degenerate points (black circles) is shown. The number of simulation elements is 153,133 ('femur'), 70,042 ('hook'), 449,918 ('wrench') and 95,028 ('bracket').

5 Results

We use several examples to compare the mechanical properties of PSL-guided material layouts to the layouts generated by density-based topology optimization with and w/o PSL-guided material initialization. All experiments have been carried out on a desktop PC with an Intel Xeon CPU at 3.60GHz. The used operations have been implemented in MatLab, to ease the combination of finite element stress analysis with PSL integration and

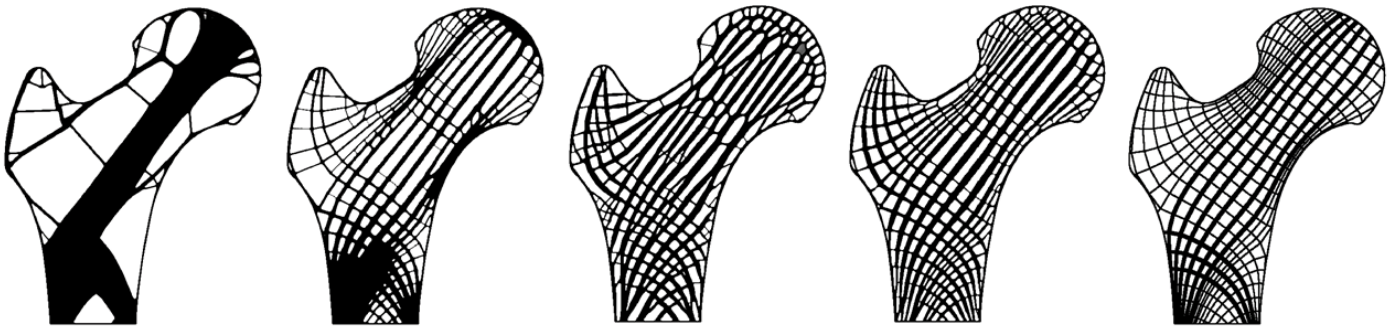

(a) $c = 1.711c_0, v = 0.500$, $s = 6.6 \times 10^{-3}, N = 281$. (b) $c = 1.764c_0, v = 0.500$, $s = 7.8 \times 10^{-3}, N = 281$. (c) $c = 2.048c_0, v = 0.539$, $s = 1.6 \times 10^{-2}, N = 1000$. (d) $c = 1.997c_0, v = 0.540$, $s = 9.9 \times 10^{-3}, N = 313$. (e) $c = 2.035c_0, v = 0.506$.

FIGURE 6. Layouts for 'femur'. (a) Topology optimization with global volume constraint, homogeneous material initialization. (b) Same as (a) but with PSL-guided material initialization. (c) Topology optimization with local volume constraint, homogeneous material initialization. (d) Same as (c) but with PSL-guided material initialization. (e) PSL-guided material layout.

material layout. All design domains are discretized by Cartesian finite element grids with unit-size simulation elements. The Young's Modulus and Poisson's ratio are set to 1.0 and 0.3, respectively.

To analyze the convergence improvements when using PSL-guided material initialization in topology optimization, we use the sharpness measure

$$s = \frac{4}{n} \sum_e \rho_e (1 - \rho_e). \tag{7}$$

A small value of s indicates a sharper binary design of the optimized layout. To facilitate the comparison of the convergence behavior, according to [6, 15] we define that the optimization process has converged once s is less than 0.01. Thus, the convergence of different approaches can be compared easily by counting the number of iterations (N) until the sharpness value is below 0.01.

Generating the PSL-guided material layout involves a finite element analysis to compute the stresses in the solid object under load, followed by PSL extraction and material deposition along PSLs. Strain-guided thickness control requires another finite element analysis to compute the strain energy of the initial material layout. A final simulation is used to evaluate the mechanical properties of the layout. Even for the largest model 'wrench' with 449,918 simulation elements (see Fig. 5e), the entire process takes less than 30 seconds. When using the PSL-guided layout as initialization for topology optimization, only the initial finite element analysis to simulate the stress field is required. In all our examples this is performed in less than 15 seconds.

In the following, the 'femur' model shown in Fig. 5 is used to compare the results of all proposed approaches and analyse their specific properties. Figure 6 shows the generated material layouts using the same external load conditions.

In Figs. 6b,a, the results of topology optimization with global volume constraint with and w/o the proposed material initialization are compared. While the compliance and the number of optimization iterations remain almost unchanged, very different material layouts are generated. It is in particular apparent that the final layout when the specific material initialization is used contains far more fine-grained sub-structures which are distributed over the domain. In Figs. 6d,c, the comparison is with respect to topology optimization under local volume constraint with and w/o the proposed initialization strategy. In this case, even at a significantly reduced number of optimization iterations the compliance is still comparable. Furthermore, the resulting layout appears more regular and is close to a 2D quad-mesh.

From Fig. 6e it can be observed that PSL-guided material layout achieves similar compliance than topology optimization with local volume constraint, yet the layout is generated at significantly lower computational cost. While it requires only three finite element simulations to generate the final layout, even with the proposed material initialization topology optimization requires over 300 iterations of finite element simulation and material update. In addition, a very regular and uniformly distributed layout is obtained.

Besides the compliance, we also evaluate the robustness of the material layouts generated by the different approaches with respect to local damage. Therefore, we remove a small piece of material from the optimized structures, but the boundary conditions are kept the same, see the region marked by a red box in Fig. 7 left. By comparing the compliances before and after local damage is applied (see Fig. 7 right), we see that the layout generated by topology optimization under global volume constraint has the weakest robustness in the tested scenario. However, by using the proposed material initialization, the robustness is improved significantly. The result by the topology optimization under local volume constraint is robust with respect to the local

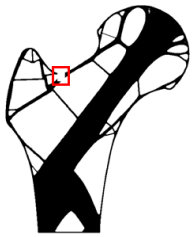

Cases in Fig. 6	Original compliance (c_0)	Compliance after local damage (c_0)
(a)	1.711	8.229
(b)	1.764	2.123
(c)	2.048	2.113
(d)	1.997	2.050
(e)	2.035	2.167

FIGURE 7. Robustness with respect to local damage. Left: Red box indicates where material is removed. Right: Compliance comparison before and after local damage. (a)-(e) correspond to the cases in Fig. 6.

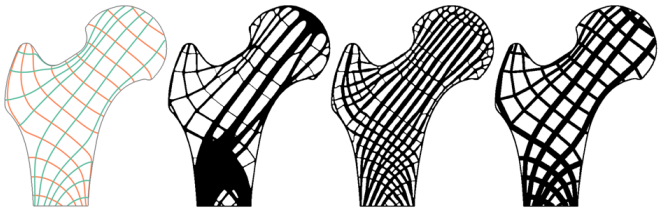

(a) PSLs (b) $c = 1.714c_0, v = 0.500$, $s = 5.8 \times 10^{-3}, N = 281$. (c) $c = 2.010c_0, v = 0.533$, $s = 1.0 \times 10^{-2}, N = 424$. (d) $c = 2.149c_0, v = 0.534$.

FIGURE 8. (a) PSLs used to guide material deposition. (b) and (c): PSL-guided material initialization of topology optimization with global and local volume constraints, respectively. (d) PSL-guided material layout with thickness control.

damage, which has also been demonstrated by the work [6], and our initialization strategy doesn't violate this feature. Furthermore, the result of using the PSL-guided structural design also shows this characteristic of the result by topology optimization under local volume constraint.

In addition to the experiments in Fig. 6 with a rather dense set of PSLs, a second row of experiments has been conducted with a more sparse set of PSLs for material initialization and PSL-guided layout (see Fig. 8a). Again, the result in Fig. 8b shows a more detailed and distributed material layout when these PSLs are used for initialization in topology optimization with global volume constraint. Figure 6c demonstrates improved convergence rate of topology optimization with local volume constraint, and Fig. 8d supports our finding that PSL-guided material layouts come at reasonably compliance yet significantly reduced computational load. On the other hand, it becomes less significant compared to Fig. 6d since less PSLs are used. In order to set an appropriate PSL distribution for the PSL-guided structural design or topology optimization, we recommend taking the affecting radius R_e in Eqn. 6 as a reference in selecting the snapping threshold ϑ of 3D-TSV, where the former determines the pore size of the porous infill, the latter controls the gaps among different PSLs.

To further demonstrate the potential of PSL-guided material initialization to improve the convergence of the optimization process, a comparison to the approach by Wang et al. [15] using only the topological skeleton of the stress field in the initialization is performed. We use the same 'bracket' model (see Fig. 5g) as in [15]. Figure 9 shows the generated material layouts and the performance statistics for both variants. While the generated layouts are similar in terms of compliance, our proposed initialization can reduce the number of optimization iterations until convergence by more than 30%.

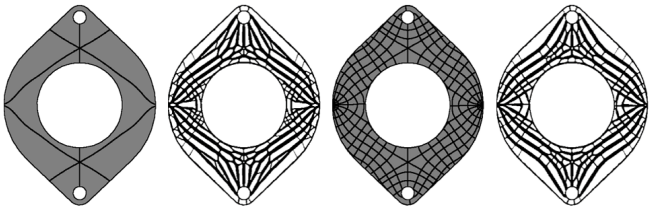

(a) Initialization by topological skeleton. (b) $c = 2.057c_0, v = 0.479$, $s = 1.0 \times 10^{-2}, N = 491$. (c) Initialization by PSLs. (d) $c = 2.094c_0, v = 0.465$, $s = 1.0 \times 10^{-2}, N = 326$.

FIGURE 9. (a), (b) Only using the topological skeleton of the stress tensor field as initial material field and the corresponding result [15]. (c), (d) The proposed approach.

By using the 'hook' and 'wrench' models, the basic features of material initialization are further emphasized (see Fig. 10). In particular, the results are in line with those obtained for 'femur', with respect to compliance and number of optimization iterations. Figure 11 shows rendering of 3D objects that were created by extruding the 2D material layouts.

6 Conclusion and future work

In this work, we have analyzed the use of PSL-guided material layouts for and as an alternative to density-based topology optimization. We have demonstrated that the convergence of topology optimization with local volume constraint can be significantly improved when such layouts are used to initialize the optimization process. When only a global volume constraint is enforced, the robustness of the final layout with respect to local damage is vastly improved. In both cases, the resulting layouts show improved regularity and are more evenly distributed across the domain.

When PSL-guided material layouts are used alone, with the thickness of PSLs adjusted according to their mechanical properties, the resulting compliances are en par with those generated by topology optimization with local volume constraint. In contrast, however, the computational complexity of the generation process is significantly reduced, and more regular and distributed layouts are generated. While compared to topology optimization with global volume constraint the overall resistance to the considered loading conditions is reduced, the layouts show significantly higher robustness to local damage. All of our experiments have shown that highly regular, smoothly varying, and distributed layouts are generated by PSL-guided material depo-

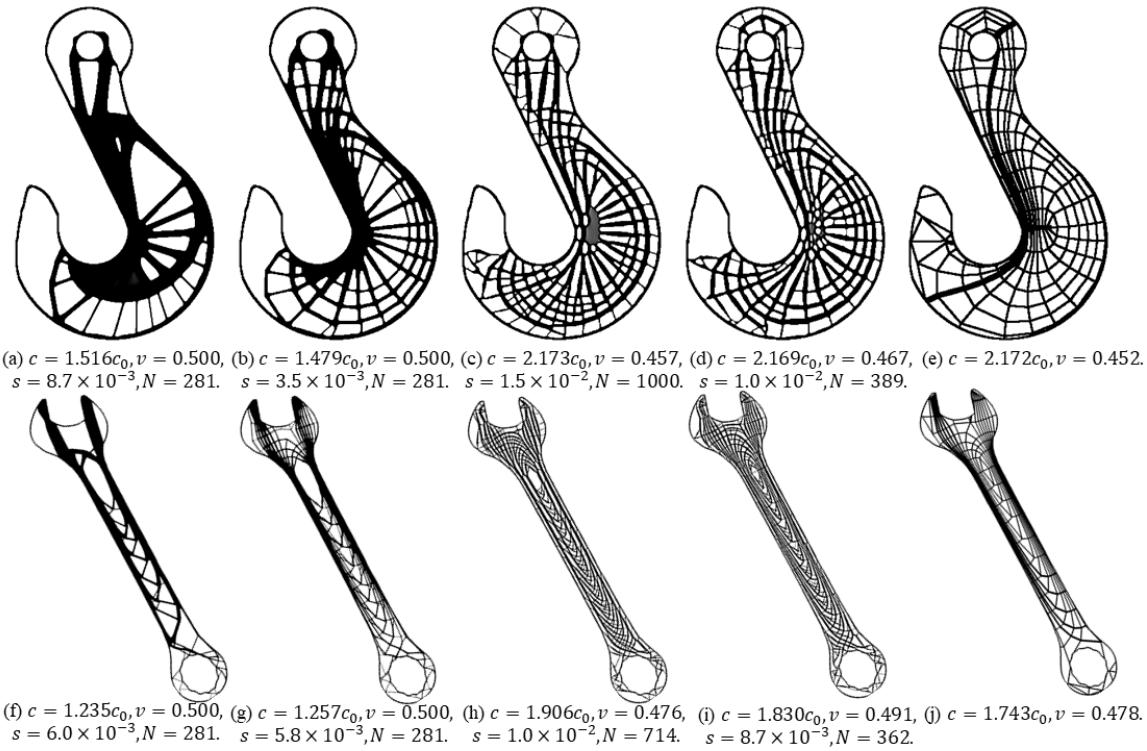

FIGURE 10. From (a) to (e), and (f) to (j), respectively: Material layouts generated via topology optimization with global volume constraint (with and w/o PSL-guided initialization), with local volume constraint (with and w/o PSL-guided initialization), and PSL-guided material layout.

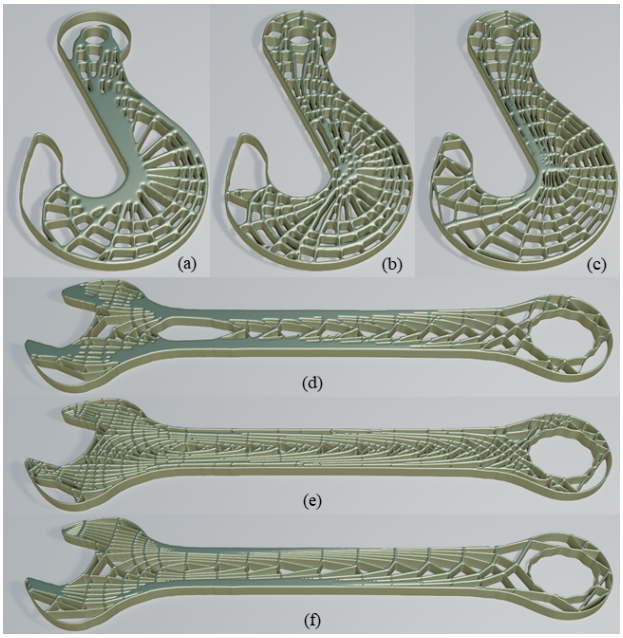

FIGURE 11. The 3D objects created by extruding the 2D designs. (a)-(f) correspond to Fig. 10b, d, e, g, i and j, respectively.

sition.

In the future, we intend to investigate the extension of PSL-guided material deposition to 3D domains. In particular, we aim at analyzing whether purely line-based structures can be obtained in 3D. Furthermore, it will be interesting to apply PSLs to compile global consistent structures from the local configuration of optimized orthotropic rectangular cells in homogenization-based topology optimization [18].

ACKNOWLEDGMENT

This work was supported in part by the German Research Foundation (DFG) under grant number WE 2754/10-1. Thanks to Christoph Neuhauser from TUM for supporting us with the 3D renderings.

REFERENCES

[1] Wu, J., Sigmund, O., and Groen, J. P., 2021. "Topology optimization of multi-scale structures: a review". *Structural and Multidisciplinary Optimization,* ***63***(3), p. 1455–1480.

[2] Bendsøe, M. P., and Kikuchi, N., 1988. "Generating optimal topologies in structural design using a homogenization

method". *Computer Methods in Applied Mechanics and Engineering,* ***71***(2), pp. 197–224.

[3] Bendsøe, M. P., 1989. "Optimal shape design as a material distribution problem". *Structural Optimization,* ***1***(4), pp. 193–202.

[4] Zhou, M., and Rozvany, G., 1991. "The COC algorithm, part ii: Topological, geometrical and generalized shape optimization". *Computer Methods in Applied Mechanics and Engineering,* ***89***(1), pp. 309–336.

[5] Mlejnek, H., 1992. "Some aspects of the genesis of structures". *Structural optimization,* ***5***(1-2), pp. 64–69.

[6] Wu, J., Aage, N., Westermann, R., and Sigmund, O., 2018. "Infill optimization for additive manufacturing – approaching bone-like porous structures". *IEEE Transactions on Visualization and Computer Graphics,* ***24***(2), February, pp. 1127–1140.

[7] Pantz, O., and Trabelsi, K., 2008. "A post-treatment of the homogenization method for shape optimization". *SIAM Journal on Control and Optimization,* ***47***(3), pp. 1380–1398.

[8] Groen, J. P., and Sigmund, O., 2018. "Homogenization-based topology optimization for high-resolution manufacturable microstructures". *International Journal for Numerical Methods in Engineering,* ***113***(8), pp. 1148–1163.

[9] Wu, J., Clausen, A., and Sigmund, O., 2017. "Minimum compliance topology optimization of shell-infill composites for additive manufacturing". *Computer Methods in Applied Mechanics and Engineering,* ***326***, pp. 358–375.

[10] Schmidt, M.-P., Pedersen, C. B., and Gout, C., 2019. "On structural topology optimization using graded porosity control". *Structural and Multidisciplinary Optimization,* ***60***(4), pp. 1437–1453.

[11] Das, S., and Sutradhar, A., 2020. "Multi-physics topology optimization of functionally graded controllable porous structures: Application to heat dissipating problems". *Materials & Design,* ***193***, p. 108775.

[12] Li, H., Gao, L., Li, H., Li, X., and Tong, H., 2021. "Full-scale topology optimization for fiber-reinforced structures with continuous fiber paths". *Computer Methods in Applied Mechanics and Engineering,* ***377***, p. 113668.

[13] Zhao, Z., and Zhang, X. S., 2021. "Design of graded porous bone-like structures via a multi-material topology optimization approach". *Structural and Multidisciplinary Optimization,* ***64***(8), pp. 677—698.

[14] Zhou, M., Lu, Y., Liu, Y., and Lin, Z., 2022. "Concurrent topology optimization of shells with self-supporting infills for additive manufacturing". *Computer Methods in Applied Mechanics and Engineering,* ***390***, p. 114430.

[15] Wang, J., Wu, J., and Westermann, R., 2022. "Stress topology analysis for porous infill optimization". *Structural and Multidisciplinary Optimization,* ***65***(3), pp. 1–13.

[16] Allaire, G., Geoffroy-Donders, P., and Pantz, O., 2019. "Topology optimization of modulated and oriented periodic microstructures by the homogenization method". *Computers & Mathematics with Applications,* ***78***(7), pp. 2197–2229.

[17] Groen, J. P., Wu, J., and Sigmund, O., 2019. "Homogenization-based stiffness optimization and projection of 2d coated structures with orthotropic infill". *Computer Methods in Applied Mechanics and Engineering,* ***349***, pp. 722 – 742.

[18] Wu, J., Wang, W., and Gao, X., 2021. "Design and optimization of conforming lattice structures". *IEEE Transactions on Visualization and Computer Graphics,* ***27***(1), pp. 43 – 56.

[19] Tam, K.-M. M., and Mueller, C. T., 2015. "Stress line generation for structurally performative architectural design". In 35th Annual Conference of the Association for Computer Aided Design in Architecture, ACADIA.

[20] Kwok, T.-H., Li, Y., and Chen, Y., 2016. "A structural topology design method based on principal stress line". *Computer-Aided Design,* ***80***, pp. 19–31.

[21] Daynes, S., Feih, S., Lu, W. F., and Wei, J., 2017. "Optimisation of functionally graded lattice structures using isostatic lines". *Materials & Design,* ***127***, pp. 215–223.

[22] Daynes, S., and Feih, S., 2022. "Bio-inspired lattice structure optimisation with strain trajectory aligned trusses". *Materials & Design,* ***213***, p. 110320.

[23] Wang, J., Neuhauser, C., Wu, J., Gao, X., and Westermann, R., 2021. "3D-TSV: The 3d trajectory-based stress visualizer". *arXiv preprint arXiv:2112.09202*.

[24] Delmarcelle, T., and Hesselink, L., 1994. "The topology of symmetric, second-order tensor fields". In Proceedings Visualization'94, IEEE, pp. 140–147.

[25] Hashin, Z., and Shtrikman, S., 1963. "A variational approach to the theory of the elastic behaviour of multiphase materials". *Journal of the Mechanics and Physics of Solids,* ***11***(2), pp. 127–140.

[26] Bendsøe, M. P., and Sigmund, O., 1999. "Material interpolation schemes in topology optimization". *Archive of Applied Mechanics,* ***69***(9-10), pp. 635–654.

[27] Sigmund, O., 2001. "A 99 line topology optimization code written in Matlab". *Structural and multidisciplinary optimization,* ***21***(2), pp. 120–127.

[28] Andreassen, E., Clausen, A., Schevenels, M., Lazarov, B. S., and Sigmund, O., 2011. "Efficient topology optimization in MATLAB using 88 lines of code". *Structural and Multidisciplinary Optimization,* ***43***(1), pp. 1–16.

[29] Svanberg, K., 1987. "The method of moving asymptotes—a new method for structural optimization". *International journal for numerical methods in engineering,* ***24***(2), pp. 359–373.